RESEARCH ARTICLE   **Open Access**

Broadband spin and angle co-multiplexed waveguide-based metasurface for six-channel crosstalk-free holographic projection

Zeyang Liu[1,2], Hao Gao[1], Taigao Ma[3], Vishva Ray[4], Niu Liu[2], Xinliang Zhang[2], L. Jay Guo[5*] and Cheng Zhang[1,2*]

Abstract

Metasurface-based holograms, or metaholograms, offer unique advantages including enhanced imaging quality, expanded field of view, compact system size, and broad operational bandwidth. Multi-channel metaholograms, capable of switching between multiple projected images based on the properties of illuminating light such as state of polarization and angle of incidence, have emerged as a promising solution for realizing switchable and dynamic holographic displays. Yet, existing designs typically grapple with challenges such as limited multiplexing channels and unwanted crosstalk, which severely constrain their practical use. Here, we present a new type of waveguide-based multi-channel metaholograms, which support six independent and fully crosstalk-free holographic display channels, simultaneously multiplexed by the spin and angle of guided incident light within the glass waveguide. We employ a *k*-space translation strategy that allows each of the six distinct target images to be selectively translated from evanescent-wave region to the center of propagation-wave region and projected into free space without crosstalk, when the metahologram is under illumination of a guided light with specific spin and azimuthal angle. In addition, by tailoring the encoded target images, we implement a three-channel polarization-independent metahologram and a two-channel full-color (RGB) metahologram. Moreover, the number of multiplexing channels can be further increased by expanding the *k*-space's central-period region or combing the *k*-space translation strategy with other multiplexing techniques such as orbital angular momentum multiplexing. Our work provides a novel approach towards realization of high-performance and compact holographic optical elements with substantial information capacity, opening avenues for applications in AR/VR displays, image encryption, and information storage.

Keywords Metasurface, Multi-channel metahologram, Color metahologram, Waveguide display

*Correspondence:
L. Jay Guo
guo@umich.edu
Cheng Zhang
cheng.zhang@hust.edu.cn
[1] School of Optical and Electronic Information, Huazhong University of Science and Technology, Wuhan 430074, China
[2] Wuhan National Laboratory for Optoelectronics, Huazhong University of Science and Technology, Wuhan 430074, China
[3] Department of Physics, University of Michigan, Ann Arbor, MI 48109, USA
[4] Lurie Nanofabrication Facility, Department of Electrical Engineering and Computer Science, University of Michigan, Ann Arbor, MI 48109, USA
[5] Department of Electrical Engineering and Computer Science, University of Michigan, Ann Arbor, MI 48109, USA

1 Introduction

Metaholograms, which can project holographic images by modulating an incident light through a two-dimensional array of artificial meta-atoms, outperform conventional holograms in terms of imaging quality, field of view, system compactness, and operational bandwidth [1–4]. Metaholograms are considered as one of the next-generation display technologies and have exhibited great potential in an array of applications such as AR/VR display [5–11], image encryption [12–16], and optical anti-counterfeiting [17–19]. For many of the above research endeavors, a key focus is to expand the device information capacity and realize

tunable metahologram operation. Towards this goal, multi-channel metaholograms have been exploited, whose projected images can switch through multiplexing different properties of an incident light including state of polarization, angle of incidence, illumination wavelength (frequency), and orbital angular momentum (OAM) [20–23].

Polarization multiplexing is one of the most common methods to implement multi-channel metaholograms. Anisotropic meta-atoms with spatially-varying geometric parameters and orientation angles have been used to construct the device, which can offer independent phase shift modulations for two arbitrarily orthogonal polarizations and support a two-channel holographic image projection [24–27]. Noise engineering is recently developed to realize an eleven-channel, single-color metahologram, but the image quality is compromised by the unavoidable crosstalk between different channels due to the dimension constraints of Jones matrix [28]. Angle-of-incidence multiplexing has been used to create two-channel metaholograms consisting of specially-designed meta-atoms, such as U-shaped and four-nanofin-assembled structures that support distinct optical resonances under illumination with two different angles of incidence [29–31]. Wavelength-multiplexing metaholograms operate based on judiciously-designed high-aspect-ratio dielectric meta-atoms, which can simultaneously provide independent phase shift modulations for discrete illumination wavelengths [32–35]. Constrained by the underlying physical mechanism or the difficulty of precise dispersion engineering for increased wavelength numbers, the afore-mentioned multiplexing methods could only provide a limited number of channels (≤ 4 in most cases) for independent holographic projection with negligible crosstalk. Although OAM multiplexing can enable metaholograms with extended projection channels, the projected images inevitably suffer from reduced spatial resolution due to pixelated spatial sampling for OAM multiplexing and compromised image quality due to the crosstalk between different OAM channels [36–38]. The above-mentioned multi-channel metahologram designs typically rely solely on the multiplexing of one state parameter of an incident light, which leads to constraints on the number of display channels and difficulties in crosstalk suppression. It is worth noting that light has intrinsically rich degrees of freedom and is jointly characterized by an array of state parameters (e.g., polarization, propagation mode, illumination angle, wavelength, etc.). Therefore, simultaneously employing multiple states of an incident light might provide a new approach to overcome the above limitations and realize high-fidelity crosstalk-free metaholograms

with extended projection channels, facilitating advanced applications such as full-color and switchable displays. Unfortunately, rational design methodologies which can effectively incorporate and multiplex several state parameters for implementing multi-channel metaholograms are still rather unexploited.

Here, we present a new type of high-fidelity multi-channel metaholograms that efficiently and concurrently multiplex two essential state parameters of an illuminating light, namely, the state of polarization and angle of incidence. Integrated atop a planar glass waveguide, the proposed metahologram consists of silicon (Si) nanopillars with spatially-varying orientation angles to enable requisite phase modulation through the geometric phase mechanism. The device supports six independent, fully crosstalk-free holographic display channels, simultaneously multiplexed by the spin state and azimuthal angle of guided light within the glass waveguide. The metahologram's *k*-space is designed to have a broad evanescent-wave region, which contains six elaborately-arranged target images. Leveraging the fundamental properties of metasurface-based holographic projection process, we derive a *k*-space translation strategy that allows each target image to be selectively moved to the center of the propagation-wave region for free-space projection without any crosstalk, when the metahologram is illuminated by a guided light with specific spin and azimuthal angle. Through adjusting the encoded target images, we further demonstrate a three-channel polarization-independent metahologram and a two-channel full-color (RGB) metahologram. In addition, the number of multiplexing channels can be increased by expanding the *k*-space's central-period region. Moreover, such *k*-space translation strategy based multiplexing approach is compatible with other multiplexing techniques such as OAM multiplexing. As a proof of concept, we demonstrate an eighteen-channel metahologram multiplexed by the state of polarization, angle of incidence, and OAM simultaneously. This work establishes a new paradigm for realizing high-performance metaholograms with expanded information capacity, facilitating various applications in dynamic holographic display, AR/VR display, image encryption, information storage, etc.

2 Results

The schematic of the proposed multi-channel metahologram is shown in Fig. 1. The device is located on top of a planar glass slab, which functions as a two-dimensional (2D) flat waveguide to guide illumination light by total internal reflection (TIR). The metahologram, designed to operate in the Fraunhofer diffraction region, can

Fig. 1 Schematic of six-channel crosstalk-free holographic image projection over a broad visible range by the spin and angle co-multiplexed waveguide-based metahologram. Each of the six independent images (e.g., capital letters with different colors shown in the schematic) can be selectively projected into the far field when the metahologram is illuminated by a guided incident light with certain spin state and azimuthal angle

selectively project six independent and crosstalk-free images according to the spin state and azimuthal angle of guided illumination light over the visible region.

2.1 Operational mechanism

For a far-field-projection metahologram working in the Fraunhofer diffraction region, the light field on the image plane, U_i, is the Fourier transform (FT) of the modulated light field on the metahologram plane, U_h,

$$U_i(f_x, f_y) = F(U_h(x, y)), \tag{1}$$

where F denotes the Fourier transform, and (x, y) and (f_x, f_y) are the 2D coordinate on the metahologram plane and image plane, respectively. Here, f_x and f_y also denote the spatial frequencies of the metahologram-modulated light field along the x and y axis, and are related to the free-space wave vector components, k_x and k_y, along the two perpendicular axes by Eq. 2.

$$\begin{cases} f_x = \frac{k_x}{2\pi} \\ f_y = \frac{k_y}{2\pi} \end{cases} \tag{2}$$

According to Eq. 1, the intensity pattern I_i of the displayed holographic image is determined by the spatial frequency distribution of the modulated light field in its Fourier space (k-space), i.e., $I_i = |U_i(f_x, f_y)|^2$. In the case of metasurface-based holographic projection, the incident light is modulated by 2D discrete meta-atoms arrayed over a pitch of P. Consequently, such metasurface-induced Fourier transform is indeed a discrete Fourier transform (DFT) with a sampling interval of P. Based on the properties of DFT, the spatial frequency distribution is a continuous and periodic function with a period of $1/P$ in two perpendicular directions (f_x, f_y), whose central period ranges from $-1/2P$ to $1/2P$ along each axis.

For the ease of description of the employed k-space in this study, we choose to utilize a new coordinate system using normalized wave vector components, (k_x/k_0, k_y/k_0), as two coordinate axes in the subsequent discussion. In this new normalized k-space coordinate system, the central-period region of the spatial frequency distribution will instead range from $-\lambda_0/2P$ to $\lambda_0/2P$, where λ_0 is the free-space wavelength of incident illumination light. Considering a metahologram whose constituent meta-atom pitch P is smaller than $\lambda_0/2$, the maximum coordinate value of the central-period spatial frequency region will exceed one (Fig. 2a). This indicates that the central-period region now contains two parts: (*i*) the propagation-wave region (illustrated by the bright area of the image plane, Fig. 2) with its boundary defined by $(k_x/k_0)^2 + (k_y/k_0)^2 = 1$, and (*ii*) the evanescent-wave region (illustrated by the shadow area of the image plane, Fig. 2) outside the above boundary. In this situation, only the spatial frequency distribution pattern inside the propagation-wave region can be observed in the far field and forms the projected holographic image, while the pattern inside the evanescent-wave region cannot reach the far field.

When the metahologram is illuminated by an oblique incident light (Fig. 2b), the spatial frequency distribution pattern in the k-space will undergo a directional translation of distance $d_t = p_g/k_0$ [39, 40],
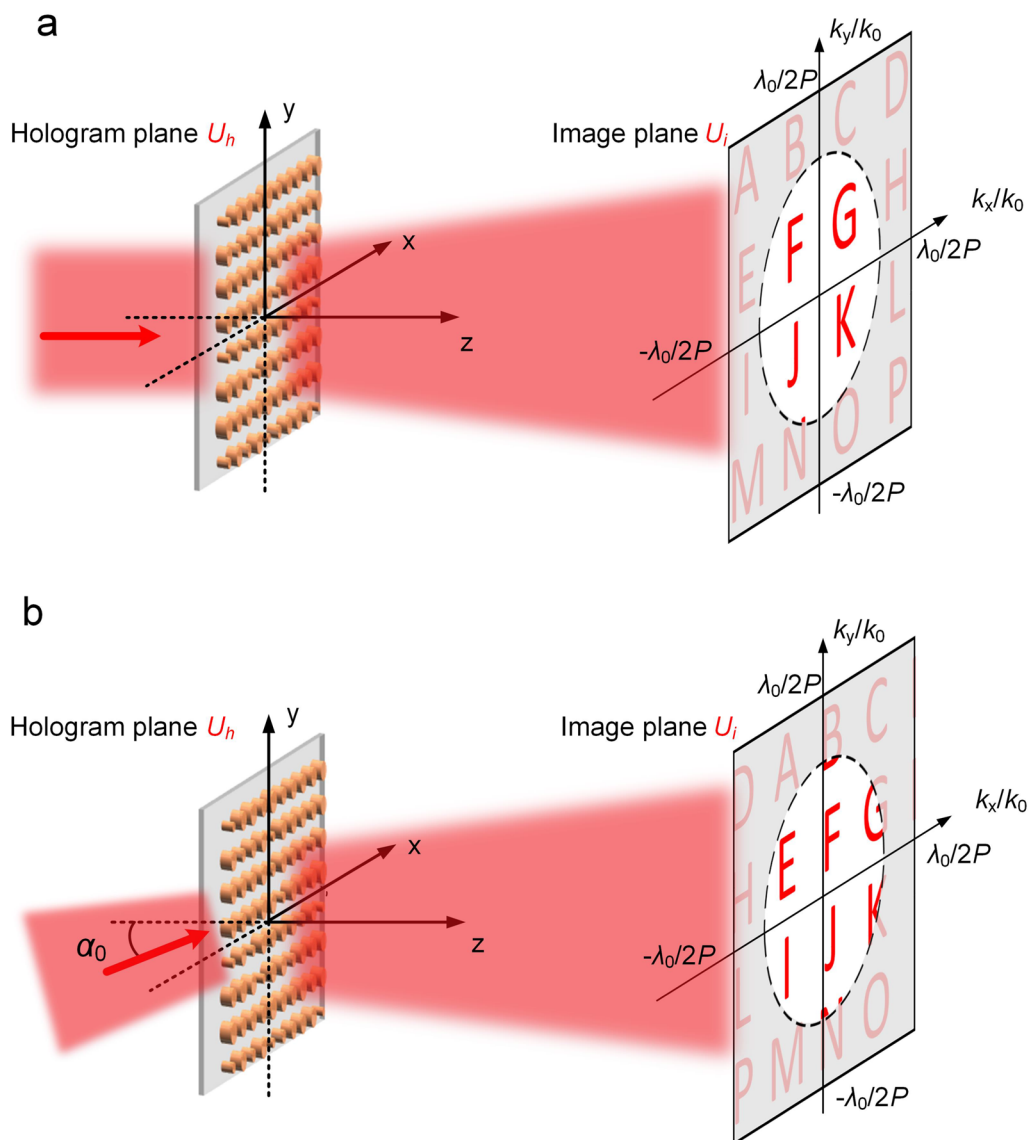
Fig. 2 Schematics of the holographic image projection by a metahologram under normal incident illumination (**a**) and oblique incident illumination (**b**). The projected far-field image (i.e., spatial frequency distribution pattern) contains sixteen equally-spaced capital letters. The pitch of the constituent meta-atoms is chosen to be $\lambda_0/3$. Consequently, the central-period region of the spatial frequency distribution pattern ranges from -1.5 to 1.5 along the two perpendicular coordinates k_x/k_0 and k_y/k_0 in the normalized k-space coordinate system. The bright area and the shadow area on the image plane indicate the propagation-wave region and evanescent-wave region, respectively. The black dashed-line circle, defined by $(k_x/k_0)^2 + (k_y/k_0)^2 = 1$, indicates the boundary between the above two regions. The propagation direction of the oblique incident light in (b) is in the x–z plane and towards the positive x axis, making an angle of α_0 with respect to the metahologram's normal direction. As an example, in the case of $\alpha_0 = 60°$, the oblique incident light imparts an in-plane phase gradient of π/λ_0 along the x axis and leads to a translation distance of 0.5 for the spatial frequency distribution pattern in the normalized k-space. After such translation, the images of capital letters "E" and "I" are moved into the propagation-wave region and the images of capital letters "G" and "K" are partially moved out of the propagation-wave region. Also, the images of capital letters "D", "H", "L" and "P" are moved out of the central-period region and appear again from the opposite side due to the periodicity of the spatial frequency distribution

$$U_i\left(\frac{1}{\lambda_0}\left(\frac{k_x}{k_0} - \frac{p_g}{k_0}cos(\theta_x)\right), \frac{1}{\lambda_0}\left(\frac{k_y}{k_0} - \frac{p_g}{k_0}cos(\theta_y)\right)\right) = F\left(U_h(x,y)exp\left(ip_g\left(xcos(\theta_x) + ycos(\theta_y)\right)\right)\right),$$

(3)

where p_g is the induced in-plane phase gradient, and θ_x (θ_y) is the angle between the direction of the in-plane phase gradient and the coordinate axis, x (y), on the metahologram plane. Detailed analysis is elaborated in Additional file 1: Part 1. With proper translation distance and direction, patterns inside the evanescent-wave region can be laterally translated into the propagation-wave region along the direction of the in-plane phase gradient. It is worth noting that because the spatial frequency distribution is periodic, when certain patterns are translated out of the central-period region, the same patterns in the adjacent regions will be moved into the central-period region from the opposite side. Therefore, by controlling the spatial angle and direction of an incident illumination light, the spatial frequency distribution pattern inside the propagation-wave region (i.e., the displayed holographic image) can be freely switched.

2.2 Device design

According to the earlier discussion, the spatial frequency distribution of a metasurface-modulated light field is both continuous and periodic. Moreover, the displayed holographic image (spatial frequency distribution pattern inside the propagation-wave region) can be freely switched by varying both the spatial angle and incident direction of the illumination light, based on the *k*-space translation strategy. Leveraging these basic properties, we propose a six-channel crosstalk-free waveguide-based metahologram co-multiplexed by spin state and azimuthal angle of the incident illumination light inside the waveguide. The central-period spatial frequency distribution patterns encoded on the metahologram for normal incident illumination are displayed in Fig. 3. Considering a red illumination light ($\lambda_0 = 637$ nm) and a chosen meta-atom pitch (*P*) of 177 nm, the central-period region of the spatial frequency distribution pattern will range from -1.8 to 1.8 ($\lambda_0/2P = 1.8$) along the two perpendicular coordinate axes, (k_x/k_0, k_y/k_0), in the normalized *k*-space. Six images (capital letters from "A" to "F"), each of which is centered on one vertex of a regular hexagon (green dashed lines) with a side length of 1.2 in the normalized *k*-space coordinate system, are chosen as the target holographic images. Each image is located inside a circular area with a radius $r_i = 0.2$ (red dashed-line circles, Fig. 3). The circular area corresponds to a divergent angle $\theta = 2arctan(r_i) \approx 22.6°$ for target images when they are selectively moved to the *k*-space center (origin of
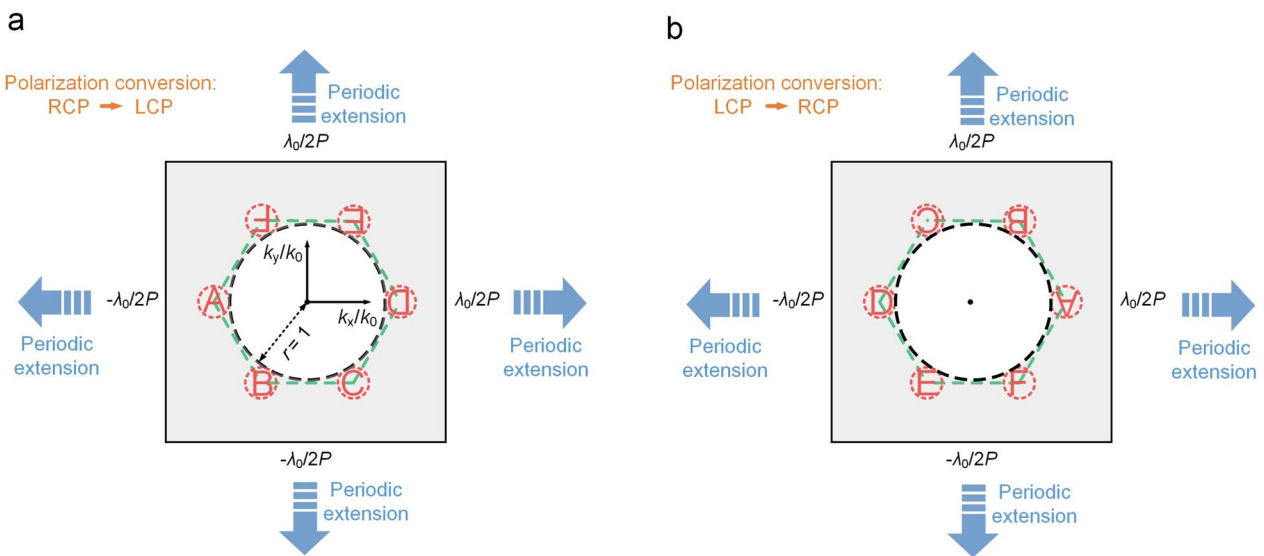

Fig. 3 Central-period spatial frequency distribution patterns encoded on the metahologram for normal incident illumination under polarization conversion from right circular polarization (RCP) to left circular polarization (LCP) (**a**) and from LCP to RCP (**b**), respectively. The two patterns, each containing six target images (capital letters from "A" to "F" inside the red dashed-line circles with a radius of 0.2), are central symmetric with respect to the origin due to the properties of the employed geometric phase modulation method. These six target images are outside the black dashed-line circle and are centered on each vertex of a regular hexagon (green dashed lines) with a side length of 1.2 in the normalized *k*-space coordinate system. The bright area and the shadow area indicate the propagation-wave region and evanescent-wave region, respectively. The black dashed-line circle denotes the boundary of the two regions and is described by $(k_x/k_0)^2 + (k_y/k_0)^2 = 1$. Due to the property of discrete Fourier transform, the entire spatial frequency distribution pattern in the *k*-space is a periodic extension of the central-period spatial frequency distribution pattern along the two perpendicular coordinate axes

k-space coordinate system) for projection in the normal direction. The center of the regular hexagon is at the origin (0, 0) of the *k*-space coordinate system, such that the center of each target image has a distance $d = 1.2$ away from the origin.

The central-period spatial frequency distribution pattern is encoded onto the metahologram by employing the geometric phase modulation method. Geometric phase typically applies to cases where a circularly-polarized light interacts with an array of anisotropic meta-atoms with the same size but different in-plane orientation angles. Phase shift modulation, which is twice the meta-atom's orientation angle, is imparted onto the converted cross-circularly-polarized light. For two circularly-polarized incident light with opposite spins, the metasurface-imparted phase shift modulations are identical in magnitude but opposite in sign. Consequently, their associated spatial frequency distribution patterns in the *k*-space are central-symmetric with respect to each other [41]. When the metahologram is under normally-incident illumination, all six target images are located outside the propagation-wave region's boundary (black dashed-line circle, Fig. 3), and therefore, cannot be projected into the far field.

Utilizing the proposed *k*-space translation strategy, each letter can be selectively moved to the center of the propagation-wave region and forms the target holographic image, as long as a translation distance $d_t = 1.2$ is provided when the metahologram is under oblique illumination by a guided light inside the glass slab. This suggests the guided incident light to impart an in-plane phase gradient $p_g = d_t \cdot k_0 = 1.2k_0$. The propagation direction of a certain guided light inside the glass slab can be described by two angles: the TIR angle α and the azimuthal angle β. Considering the glass slab waveguide has a refractive index $n_g \approx 1.46$ at the device operational wavelength $\lambda_0 = 637$ nm, the afore-mentioned phase gradient leads to a TIR angle $\alpha = arcsin(p_g/k_0 n_g) \approx 55.3°$. This calculated angle is greater than the critical TIR angle $\alpha_c = arcsin(1/n_g) \approx 43.2°$, and therefore, the required in-plane phase gradient can be offered by stable guided light inside the glass slab. It is worth noting that the value of the resulting translation distance equals the effective index of a guided illumination light, and an arbitrary translation distance between 1 and n_g can be readily provided through varying the TIR angle α. Moreover, an even wider range of translation distance can be offered by employing waveguide slabs made of higher refractive index materials (e.g., SiC, TiO$_2$, GaN, SiN$_x$, etc.).

The distance of *k*-space lateral translation is determined by the TIR angle α of the guided incident light, while the direction of such translation is decided by the azimuthal angle β. For the designed metahologram,

by fixing $\alpha = 55.3°$ and choosing discrete β values from 0° to 300° with a step of 60°, each target image can be selectively translated to the center of propagation-wave region for far-field projection while all the other images are still confined in the evanescent-wave region and remain as "hidden" for far-field observation. Moreover, the employed geometric phase modulation method further enriches the metahologram's functionality with spin multiplexing. When the illumination light switches circular handedness and undergoes opposite polarization conversion, the three pairs of capital letters on two opposite vertices of the regular hexagon are mutually switched (Fig. 3). Therefore, when the designed waveguide-based metahologram is imparted the same required in-plane phase gradient (determined by α and β of the guided incident light), simply flipping the spin of the circularly-polarized guided incident light will lead to a switch between a pair of target images "A" and "D", "B" and "E", or "C" and "F". Using such configuration, a six-channel crosstalk-free metahologram co-multiplexed by spin and azimuthal angle of guided incident light can be readily implemented. As shown in Fig. 4, depending on the combinations of spin state (RCP or LCP) and azimuthal angle β (0°, 60°, or 120°) of guided incident light, different target images (capital letters "A" to "F") can be selectively translated to the *k*-space center for holographic projection along normal direction in free space, and at the same time, all other five letters are translated accordingly but still remain in the evanescent-wave region to avoid crosstalk between channels.

By simultaneously employing the *k*-space translation strategy based on the fundamental properties of DFT and the geometric phase encoding method widely used in diverse metasurface designs, we have developed a spin and angle co-multiplexed waveguide-based metahologram. This device enables the projection of six independent images without any crosstalk, precisely determined by the incident azimuthal angle β and the spin state of the guided incident light. It is worth noting that in the previous discussion, six capital letters are selected as target holographic images just for the ease of description. Indeed, arbitrary images can be chosen as long as they can be arranged within a circular area with a radius of 0.2 in the normalized *k*-space coordinate. We also note that free-space oblique light illumination has recently been adopted to translate target images in the *k*-space for high-information-capacity metaholograms [39, 40]. However, such free-space illumination schemes cannot provide phase gradient greater than k_0 and therefore lack support for multi-channel crosstalk-free holographic projection. Specifically, when a certain target image is translated to the center of propagation-wave region for holographic image formation along the normal direction, other target
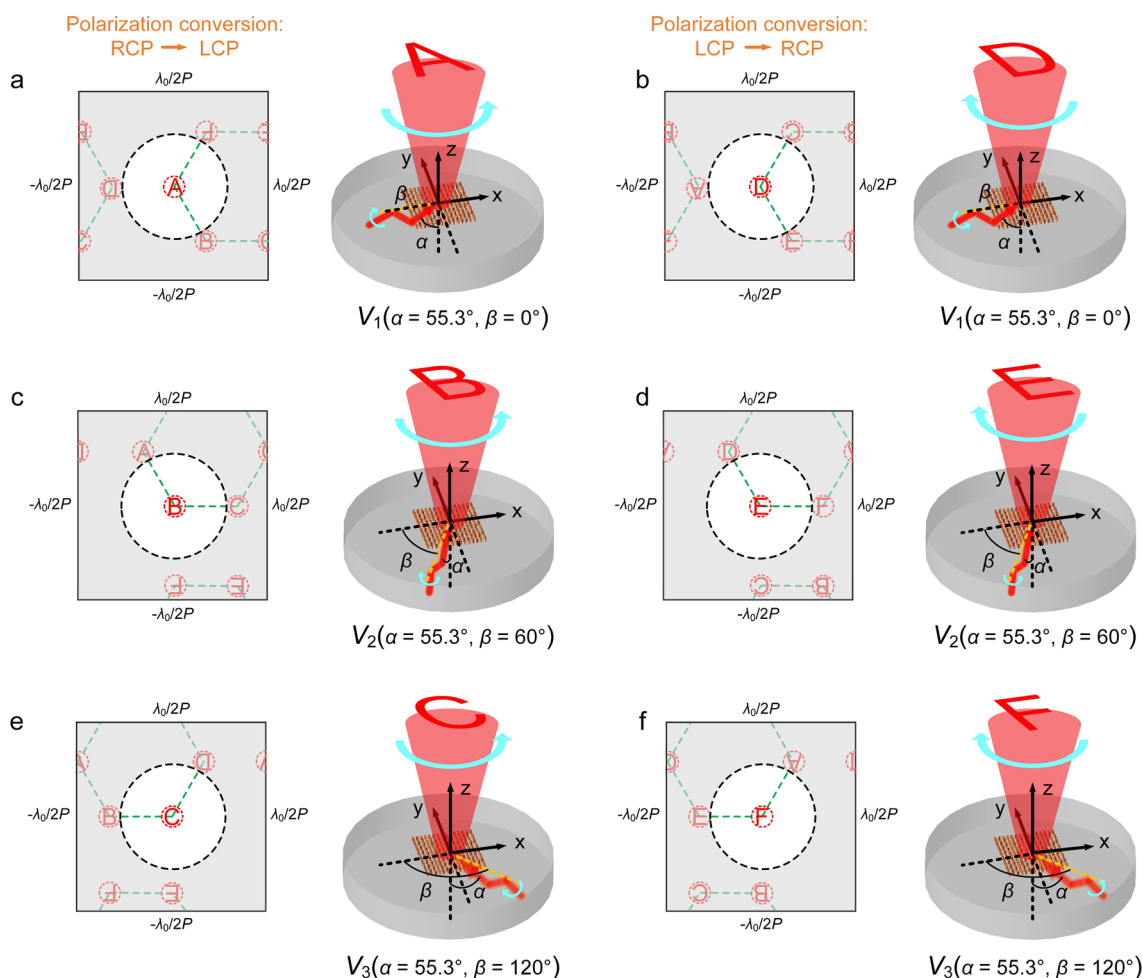
Fig. 4 Operational mechanism of the six-channel metahologram. **a**–**f** Central-period spatial frequency distribution patterns (left panel in each figure) and corresponding holographic projection schematics (right panel in each figure) for the metahologram under guided light illumination ($\alpha = 55.3°$) with different azimuthal angle β and spin state. For guided illumination light having different spin states (RCP and LCP) and propagating along different designed directions V_1 ($\alpha = 55.3°$, $\beta = 0°$), V_2 ($\alpha = 55.3°$, $\beta = 60°$) and V_3 ($\alpha = 55.3°$, $\beta = 120°$), different target images can be selectively translated to the center of the propagation-wave region and get projected into the far field; while all other five letters are translated accordingly but still remain in the evanescent-wave region. Here, α denotes the guided light's TIR angle and β denotes the guided light's azimuthal angle with respect to the positive x-axis

images remain in the propagation-wave region and get projected along off-normal directions. In contrast, the total internal reflection (TIR) illumination scheme proposed in this work overcomes the above limitation by readily providing phase gradient greater than k_0, making it well-suited for constructing high-fidelity and crosstalk-free multi-channel metaholograms. Moreover, such TIR illumination scheme, wherein the illumination light is conveyed through TIR inside a thin and compact glass slab, prevents unmodulated residual light from directly transmitting into free space and offers compatibility with on-chip as well as glass-like AR displays.

2.3 Numerical verification

To implement the proposed waveguide-based metahologram, each constituent meta-atom is designed to comprise a rectangular poly-silicon (poly-Si) nanopillar with a lattice pitch P of 177 nm (Fig. 5a). The meta-atoms are expected to convert the spin of circularly-polarized incident light and impart phase modulation on the converted cross-circularly-polarized light to form the corresponding holographic image in the device's far field. The nanopillar's structural parameters are optimized based on the cross-polarization conversion efficiency for normal incident illumination. Different combinations of pillar height and cross-sectional size are evaluated to find a proper combination that leads to a reasonable cross-polarization conversion efficiency across the visible region. After
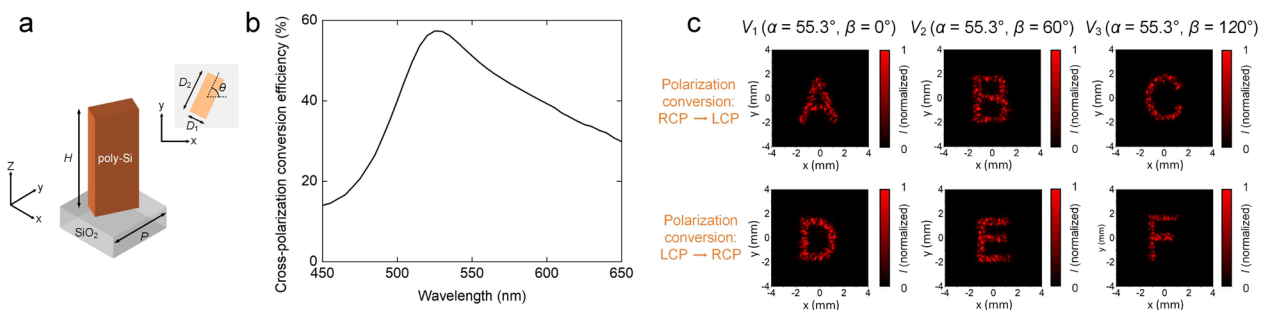
Fig. 5 Numerical verification of the six-channel metahologram. **a** Schematic of the constituent meta-atom, which comprises a poly-Si nanopillar with height $H = 280$ nm, rectangular cross-section (side lengths $D_1 = 120$ nm and $D_2 = 50$ nm), and rotation angle θ, arranged on a SiO$_2$ substrate to form a square lattice with a subwavelength lattice pitch $P = 177$ nm. Geometric phase modulation is imparted on the converted cross-circularly-polarized light via the variation in θ as a function of the nanopillar position across the device. **b** Simulated cross-polarization conversion efficiency between two opposite spin states by the meta-atom under normal light illumination. The meta-atom exhibits an acceptable broadband polarization conversion capability over the visible spectral region under study (450 nm to 650 nm). **c** Simulated holographic imaging results of the six-channel metahologram. Six crosstalk-free holographic images (capital letters "A" to "F") can be selectively projected, depending on the azimuthal angle β (0°, 60°, or 120°) and spin state (RCP or LCP) of the guided incident light ($\lambda_0 = 637$ nm) inside the glass slab. In the simulation, the metahologram consists of 200 × 200 meta-atoms and occupies a square area with a side length of 35.2 μm. The image plane is located 1 cm above the metahologram device

several rounds of iteration, the combination of pillar height ($H = 280$ nm) and cross-sectional size (long-axis length $D_1 = 120$ nm, short-axis length $D_2 = 50$ nm) is chosen, considering both the target cross-polarization conversion efficiency and the feasibility of subsequent device fabrication. Detailed analysis is elaborated in Additional file 1: Part 2. Figure 5b plots the simulated cross-polarization conversion efficiency over the visible region (450–650 nm), where the nanopillar exhibits an acceptable broadband polarization conversion capability.

We first validate our metahologram design through numerical simulation (details are elaborated in Additional file 1: Part 3). In the simulation, a metahologram having 200 × 200 meta-atoms and occupying a square area with a side length of 35.2 μm is evaluated. The aforementioned "six-capital-letter" pattern in Fig. 3 is chosen as the target spatial frequency distribution pattern, and the required phase shift modulation profile on the metahologram plane is calculated using the Gerchberg-Saxton (G-S) algorithm (details are elaborated in Additional file 1: Part 4). The spatially-varying orientation angle of each constituent poly-Si meta-atom is determined based on the geometric phase encoding method. Figure 5c displays the simulated holographic imaging results. As expected, six crosstalk-free holographic images are selectively projected into the far field, depending on the combination of azimuthal angle β (0°, 60°, or 120°) and spin state (RCP or LCP) of the guided incident light ($\lambda_0 = 637$ nm) inside the glass slab. We also attempt to estimate the working efficiency of the device, and the associated details are elaborated in Additional file 1: Part 5. Finally, it is worth noting that by employing visible-transparent materials (e.g., a-Si:H, TiO$_2$, Ta$_2$O$_5$, SiN$_x$, etc.) [14, 24, 42,

43] or adopting advanced algorithm to further optimize the meta-atom's structural parameters [44] for implementing geometric phase on the guided incident light, the device performance might be further improved.

2.4 Experimental results

We fabricate a six-channel metahologram comprising 1500 × 1500 meta-atoms and occupying a square area with a side length of 264 μm on a 500-μm-thick fused silica substrate. Details of the device fabrication process are elaborated in the Methods. The employed target holographic image and the associated nanopillar design are the same as those of the device used in the earlier numerical validation. Figure 6a, b respectively displays the optical micrograph of the fabricated sample and the scanning electron micrograph (SEM) showing details of the poly-Si nanopillars. The sample is mounted on the center of a 5-mm-thick polished planar glass slab having a regular-hexagon shape, which is in optical contact with the sample's fused silica substrate. The optical contact is achieved by using an UV-curable resin, which provides close index matching to the fused silica substrate over the visible. In addition, all six side edges of the glass slab are polished at 35° with respect to the vertical direction for the convenience of light in-coupling into the slab from free space. A red illumination laser beam ($\lambda_0 = 637$ nm) first passes through a pair of linear polarizer (LP) and quarter-wave plate (QWP), and then gets in-coupled into the glass slab through one of its six polished side edges. The projected holographic image by the metahologram is recorded by a custom-built imaging system, whose key parts include an objective lens (NA = 0.5), a tube lens, and a complementary metal-oxide semiconductor (CMOS) camera

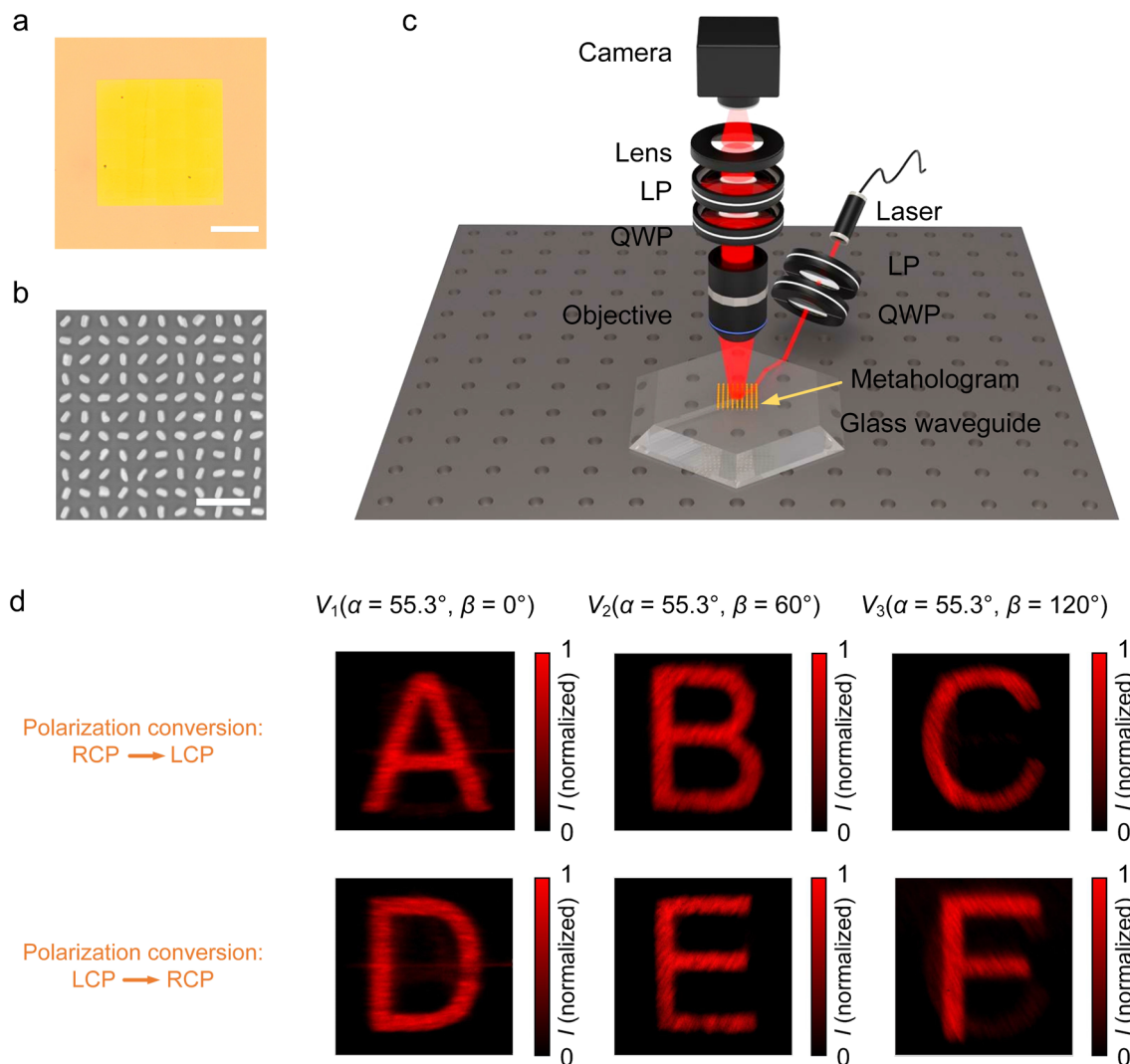**Fig. 6** Experimental results of the six-channel metahologram. **a** Optical micrograph of the fabricated metahologram. Scale bar: 100 μm. **b** Scanning electron micrograph (SEM) of the details of the fabricated metahologram. Scale bar: 500 nm. **c** Schematic of the custom-built imaging setup for recording the projected holographic images by the metahologram. QWP: quarter-wave plate. LP: linear polarizer. **d** Experimental results of holographic images projected by the metahologram. Six crosstalk-free holographic images (capital letters "A" to "F") are selectively projected when the metahologram is illuminated by a guided incident light with different azimuthal angles β (0°, 60°, and 120°) and spin states (RCP and LCP)

(Fig. 6c). More details about the custom-built imaging system are elaborated in the Methods.

In experiment, when the metahologram is respectively illuminated by a given guided incident light (with the designed TIR angle $\alpha = 55.3°$) propagating along three discrete azimuthal angles ($\beta = 0°$, 60°, 120°) and having two opposite spin states (RCP, LCP), six independent and crosstalk-free holographic images (capital letters from "A" to "F") are selectively generated and get recorded by the custom-built imaging system (Fig. 6d), showing a good correspondence with the simulation results. The divergent angle of the projected holographic image is measured to be 23.2°, showing a close correspondence to its theoretical value of

22.6°. Finally, we would like to point out that for a circularly-polarized light, its state of polarization will gradually vary as it propagates inside the glass slab. This is due to the fact that the light's two orthogonal linearly-polarized components will experience different phase shifts upon TIR at the glass-air interface according to the Fresnel Formula (detailed analysis is elaborated in Additional file 1: Part 6) [45]. To compensate for such phase shift difference and ensure that the guided light illuminating the metahologram region has the proper spin, the polarization state of the free-space incident light is adjusted to be slightly elliptical instead of circular. When the polarization of a free-space incident light is set to the proper state, the out-coupled
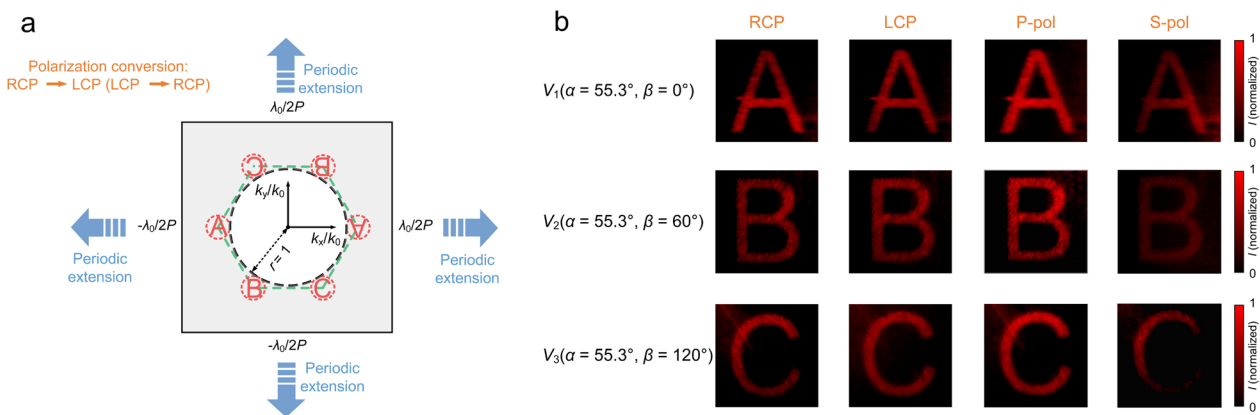
Fig. 7 Three-channel polarization-independent metahologram. **a** Central-period spatial frequency distribution pattern encoded on the three-channel polarization-independent metahologram for normal illumination. The paired two images on the opposite vertices are the same but with an in-plane rotation of 180° with respect to each other. Consequently, the pattern remains the same under polarization conversions from RCP to LCP and from LCP to RCP. **b** Experimental results of holographic image projection by the metahologram. Three crosstalk-free holographic images (capital letters "A" to "C") are selectively projected in the far field when the metahologram is illuminated by a guided incident light with different azimuthal angles β (0°, 60°, and 120°). The projected letter remains the same as the polarization state of the incident light varies. Images under four different representative states of polarization (RCP, LCP, P-pol, and S-pol) are displayed here. For the images in the same row, their intensity distributions are normalized to the maximum intensity value of all four images

imaging light from the metahologram exhibits a circular state of polarization having opposite handedness to the incident light, and at the same time, the projected holographic image shows the greatest brightness level. More details are provided in Additional file 1: Part 7.

2.5 Three-channel polarization-independent metahologram

Moreover, using the same design strategy and meta-atom structure, we can also implement a three-channel crosstalk-free polarization-independent metahologram multiplexed by the azimuthal angle β of the guided incident light. This is achieved by simply adjusting the encoded spatial frequency distribution pattern of the metahologram. Instead of having six different letters as the target images on the vertices of the regular hexagon, we now choose to employ the same letter for the paired two images on the opposite vertices and the images are further in-plane rotated 180° with respect to each other (Fig. 7a). In this way, the spatial frequency distribution pattern is central symmetric with respect to the origin, and it will remain the same regardless of the polarization state (circular, linear, elliptical, etc.) of the illumination light for such geometric-phase-based metahologram in this study. Therefore, as long as the illuminating guided light with arbitrary polarization state propagates along the proper direction to impart the required in-plane phase gradient over the metahologram, the same target image will be moved to the k-space center for far-field holographic projection.

We fabricate such three-channel polarization-independent metahologram having the same size as the earlier six-channel device and characterize the device in a similar manner. The projected images are captured using the custom-built imaging system when the metahologram is illuminated by a guided incident light propagating along one of the three azimuthal directions (V_1 to V_3). To demonstrate the device's polarization independent character, the incident light is successively set to have four typical states of polarization, namely, RCP, LCP, P-polarization (electric field vector parallel to the plane of incidence), and S-polarization (electric field vector perpendicular to the plane of incidence). More details about the measurement procedure are provided in Additional file 1: Part 8. Experimental results (Fig. 7b) show a consistent preservation of projected images across varying polarization states of the incident light, and the image can only be switched through manipulating the azimuthal angle of incident light. In addition, the projected holographic image exhibits certain discernible fluctuations in intensity for illuminating light of the same power but different states of polarization. The images are noticeably brighter when subjected to P-polarized illumination as opposed to S-polarized illumination. The brightness of images produced under two circularly-polarized illuminations is close to each other and lies intermediary between the two afore-mentioned cases. Such difference could be attributed to the fact that a P-polarized guided light has an electric field component perpendicular to the glass waveguide surface, which results in more efficient

interaction between the electric field of incident light and the meta-atoms atop the waveguide.

2.6 Dual-channel full-color metahologram

In addition to creating multi-channel crosstalk-free metaholograms having either polarization dependent or independent responses, we can extend the capability of our design by implementing a dual-channel full-color metahologram multiplexed by the spin of guided incident light, through capitalizing on the broadband response characteristic of the employed geometric phase

modulation method. Our designed metahologram is engineered to operate under the simultaneous illumination of red, green, and blue (RGB) lasers, each with free-space wavelength $\lambda_0 = 637$ nm, 532 nm, and 473 nm, respectively. The individual RGB components of two different colored images, namely "lilac" and "rose", are encoded into the two distinct sets of angle-multiplexed channels (Fig. 8a). Due to the inherent dispersive nature of the geometric phase modulation, the dimension of a projected image is proportional to the wavelength of illumination. To mitigate such effect and ensure a seamless
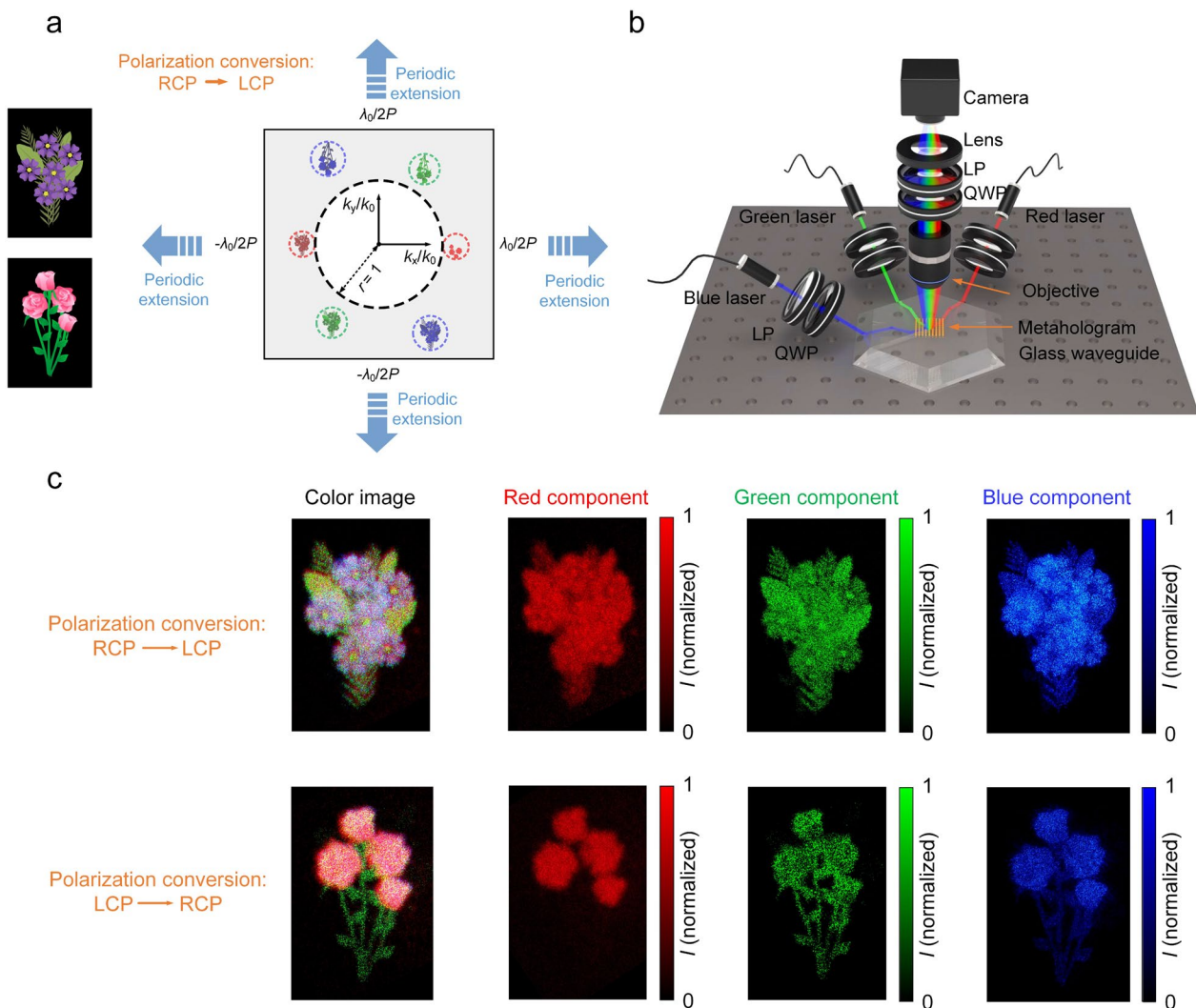

Fig. 8 Dual-channel full-color metahologram. **a** Left panel: two original colored images of flowers "lilac" and "rose". Right panel: central-period spatial frequency distribution pattern encoded on the dual-channel full-color metahologram for normal illumination under polarization conversion from RCP to LCP. **b** Schematic of the custom-built imaging system for recording the projected holographic images by the color metahologram. RGB laser beams are simultaneously coupled into the glass waveguide from three adjacent side edges and propagate along three azimuthal directions (V_1, V_2, and V_3, corresponding to $\beta = 0°$, 60°, and 120°, respectively). **c** Experimental results of holographic image projection by the full-color metahologram. Two crosstalk-free colored images are selectively projected when the metahologram is illuminated simultaneously by RGB guided incident light all having RCP or LCP spin state. The RGB components of these colored images are also captured by illuminating the metahologram with the corresponding single-color guided incident light

overlap of all projected RGB components in free space, careful adjustments are made to both the sizes and center locations of different color components in the *k*-space. A detailed account of these adjustments and the associated underlying mechanisms are elaborated in Additional file 1: Part 9.

We fabricate a dual-channel full-color metahologram having 3000×3000 meta-atoms and occupying a square area with a side length of 528 μm on a 500-μm-thick fused silica substrate, and subsequently characterize the device using the custom-built imaging system. As illustrated in Fig. 8b, RGB laser beams are simultaneously coupled into the glass waveguide from three adjacent side edges and propagate along three azimuthal directions (V_1, V_2, and V_3). As expected, the metahologram yields two distinct, crosstalk-free, and spin-multiplexed colored images (Fig. 8c), when the states of polarization of three illumination beams are properly configured as RCP or LCP. Furthermore, we capture all six RGB constituent components of the two independent colored holographic

images by illuminating the metahologram with the corresponding laser beam. The recorded images exhibit a remarkable fidelity to the original encoded ones, aligning closely with the design intent. It is worth noting that the projection of multiplexed crosstalk-free colored images through a non-interleaved metahologram holds immense potential for a wide array of advanced display applications [46–48], and has so far remained largely elusive in prior endeavors. The dual-channel, full-color metahologram we present herein represents an innovative and effective approach along this route.

2.7 Eight-channel metahologram

We have demonstrated several high-performance, six-channel crosstalk-free metaholograms using the proposed *k*-space translation strategy. Indeed, such design methodology is universal and can be employed to realize metaholograms hosting more crosstalk-free projection channels by further expanding the *k*-space's central-period range to properly accommodate more
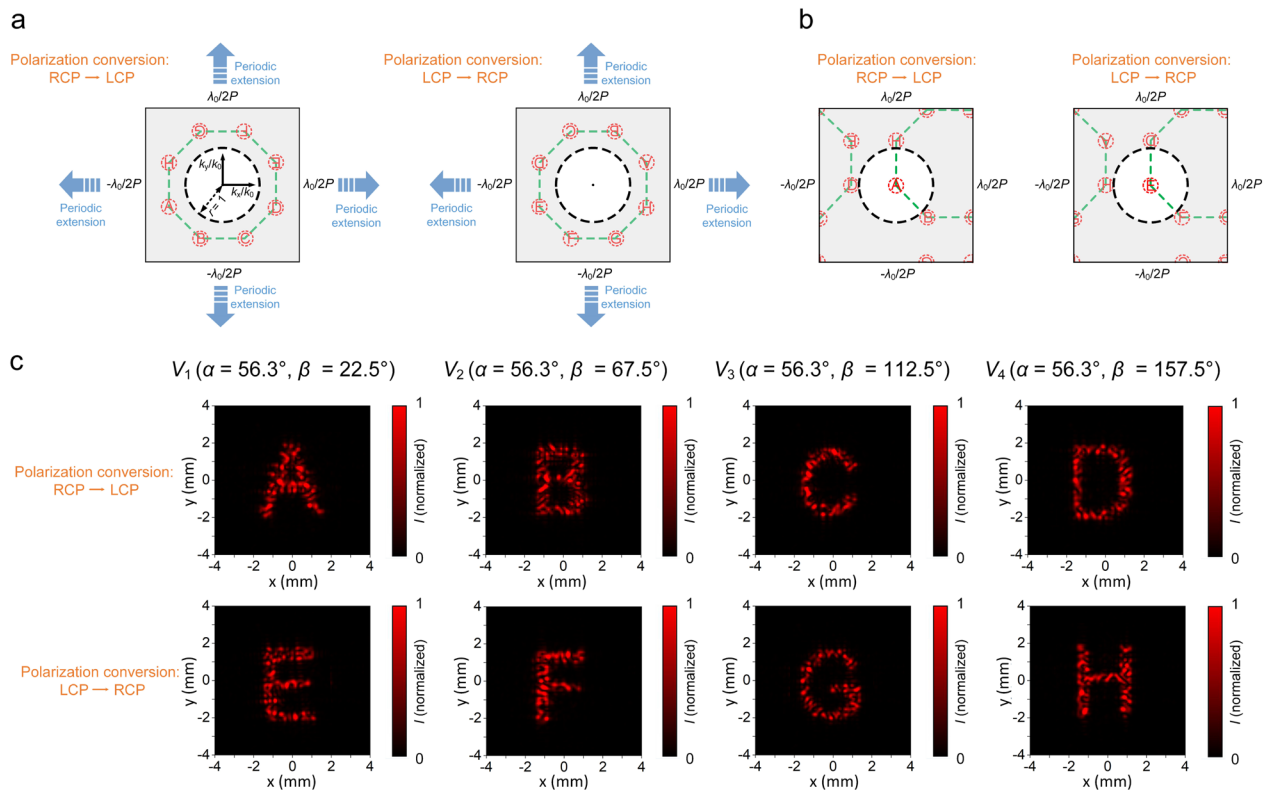

Fig. 9 Numerical verification of the eight-channel metahologram. **a** Central-period spatial frequency distribution patterns encoded on the eight-channel metahologram for normal incident illumination under polarization conversion from RCP to LCP (left panel) and from LCP to RCP (right panel), respectively. **b** Central-period spatial frequency distribution patterns for guided light illumination ($\alpha = 55.7°$, $\beta = 22.5°$) under polarization conversion from RCP to LCP (left panel) and from LCP to RCP (right panel), respectively. When the target image "A" or "E" is moved to the *k*-space center, all other target images are translated accordingly but still remain in the evanescent-wave region. **c** Simulated holographic imaging results of the eight-channel metahologram. Eight crosstalk-free holographic images (capital letters "A" to "H") are selectively projected in the far field depending on the azimuthal angle β (22.5°, 67.5°, 112.5°, or 157.5°) and spin (RCP or LCP) of the guided incident light inside the glass slab

target images. As an example, we now implement an eight-channel device and evaluate its performance through numerical simulation. Similar to the case of six-channel metahologram, the device's eight target images are designed to locate on the vertices of a regular octagon with a side length of 1.2, whose center is located at the origin of the normalized k-space coordinate system (Fig. 9a). Each target image is located inside a circular area with a radius $r_i = 0.2$, and the center of each image has a distance $d \approx 1.57$ away from the origin. To ensure that all remaining images are still outside the propagation-wave region when a given target image is translated to the k-space center, the central-period region is now chosen to range from -2.05 to 2.05 along the two coordinate axes (k_x/k_0 and k_y/k_0). Associated design details are elaborated in Additional file 1: Part 10. Consider the same free-space illuminating wavelength $\lambda_0 = 637$ nm, the designed range of the central-period region leads to a meta-atom pitch of 155 nm. To still employ poly-Si as the constituent material and the geometric phase modulation as the encoding method, the structural parameters (D_1, D_2, H) of the nanopillar are optimized as (110 nm, 40 nm, 280 nm).

In order to move a given target image to the k-space center for holographic projection normal to the device plane, a translation distance $d_t = d \approx 1.57$ is required. Such translation distance corresponds to an in-plane phase gradient $p_g = d_t \cdot k_0 \approx 1.57\ k_0$, which suggests that the planar waveguide needs to have a refractive index larger than 1.57. This can be easily accommodated by using high-refractive-index glass, which have already been employed for manufacturing waveguide components in large-FOV AR displays [49, 50]. In this study, we select Schott N-LASF46 as the waveguide material, which exhibits an index $n_g \approx 1.90$ at the metahologram operating wavelength $\lambda_0 = 637$ nm. The illuminating guided light will be conveyed inside the Schott N-LASF46 glass waveguide by a TIR angle $\alpha = arcsin(p_g/k_0 n_g) \approx 56.3°$. For such metahologram, when the guided illuminating light has a proper azimuthal angle β (22.5°, 67.5°, 112.5°, or 157.5°), and a circular polarization (RCP or LCP), one of the eight target images can be selectively moved to the k-space center and get projected normally off the metahologram, while all other target images remain in the evanescent-wave region. Figure 9b shows the central-period spatial frequency distribution patterns for $\beta = 22.5°$ as an example. By varying the azimuthal angle and spin state of the guided incident light, the designed metahologram can project eight crosstalk-free holographic images into the far field (Fig. 9c). More details of the simulation process are elaborated in Additional file 1: Part 10.

3 Discussion

We would like to highlight that the proposed k-space translation strategy is also compatible with other multiplexing techniques such as OAM multiplexing. In this way, the number of display channels can be significantly extended. As a proof of concept, we employ three OAM light beams respectively with topological charges [51] (an integer number of 2π phase changes on a closed loop around the optical vortex) ranging from 1 to 3 and demonstrate an eighteen-channel metahologram multiplexed by state of polarization, angle of incidence, and OAM simultaneously. The associated details are elaborated in Additional file 1: Part 11.

In conclusion, our study introduces an innovative class of waveguide-based multi-channel metaholograms capable of projecting six independent and crosstalk-free holographic images when illuminated by a guided light featuring different combinations of spin state and azimuthal angle. Expanding on the proposed k-space translation strategy, we also showcase three-channel polarization-independent metaholograms and two-channel full-color metaholograms. Furthermore, we illustrate the potential of extending the number of multiplexing channels by expanding the k-space's central-period region or combining the k-space translation strategy with other multiplexing techniques such as OAM multiplexing. In comparison to previously reported multi-channel metahologram designs which typically utilize one single state parameter, our design can simultaneously and effectively employ two fundamental state parameters of incident light—angle of incidence and state of polarization, and excel in hosting a greater number of display channels, eliminating inter-channel crosstalk, and unlocking various functionalities including polarization-multiplexed display, polarization-independent display, and full-color (RGB) display. Moreover, by the simple fact that only the metahologram-modulated light gets coupled out of the waveguide slab to form the projected image, our device is free of directly-transmitted residual light, a common issue in many metaholograms. This work provides a novel route towards creating metaholograms with enhanced information capacity and improved imaging fidelity, and hold substantial promise for diverse applications in compact display and information storage devices.

4 Methods

4.1 Device fabrication

A 280-nm-thick poly-Si layer is deposited on fused silica substrate through low pressure chemical vapor deposition (LPCVD). A ~ 75-nm-thick layer of negative tone hydrogen silesquioxane (HSQ) resist derived from dry

silica resin (H-SiO$_x$) in Methyl isobutyl ketone (MIBK) carrier solvent is spin-coated on the substrate, followed by a 120°C bake for 2 min for high contrast and sensitivity at low exposure dose. Then, a ~ 40-nm-thick anti-charging layer (DisCharge H$_2$O) is spin-coated on the substrate. A 100 keV electron beam lithography system is used to expose the metasurface patterns. After the exposure, the anti-charging layer is removed by soaking the sample in deionized (DI) water for 45 s with gentle agitation, followed by drying off in compressed ultra-pure N$_2$ gas. The electron beam resist is developed by soaking the sample in 2.2% tetramethylammonium hydroxide (TMAH) solvent for 45 s, followed by DI water rinsing for 30 s and ultra-pure N$_2$ gas drying. Using the developed HSQ layer as the etch mask, inductively coupled-plasma (ICP) reactive ion etching is performed to transfer the metasurface pattern into the poly-Si layer. After the ICP etching, the residual HSQ layer is estimated to be less than 20 nm in thickness, which possesses minimal influence over the metasurface performance. The associated details are elaborated in Additional file 1: Section Part 12. The metasurface fabrication process concludes with cleaning the sample successively with solvent soaking and oxygen (O$_2$) plasma treatment.

4.2 Device characterization

To characterize the metahologram, we employ a continuous-wave (CW) semi-conductor laser ($\lambda_0 = 637$ nm) as the red-light source, and two CW diode-pumped solid-state lasers ($\lambda_0 = 532$ nm and 473 nm) as the green- and blue-light sources, respectively. Broadband polarizers and quarter-wave plates that can operate over the visible range are used in the custom-built imaging system to modulate the polarization state of incident light. A complementary metal–oxide–semiconductor (CMOS) camera that can response over the visible and capture 12-bit full-color images with a resolution of 3072 × 2048 is used to record the projected holographic images.

Supplementary Information

The online version contains supplementary material available at https://doi.org/10.1186/s43593-024-00063-9.

Additional file 1. Part 1. Translation distance of spatial frequency pattern for oblique light illumination. **Part 2.** Structural parameter optimization of the meta-atom. **Part 3.** Holographic imaging simulation of the six-channel metahologram. **Part 4.** The Gerchberg–Saxton algorithm used in the metahologram design. **Part 5.** Simulated operational efficiency of the waveguide-based metahologram. **Part 6.** Phase changes of P- and S-polarized light upon total internal reflection. **Part 7.** State of polarization of free-space incident light in the six-channel holographic imaging experiment. **Part 8.** Experimental procedure of obtaining the projected holographic images by the three-channel polarization-independent metahologram. **Part 9.** Spatial frequency pattern encoded on the dual-channel full-color metahologram. **Part 10.** Design of the eight-channel

---

metahologram. **Part 11.** Extended number of display channels by orbital angular momentum multiplexing. **Part 12.** Influence of the residual hydrogen silesquioxane layer on the meta-atom's cross-polarization conversion efficiency.

References
1. Q. Jiang, G. Jin, L. Cao, When metasurface meets hologram: principle and advances. Adv. Opt. Photonics **11**, 518–576 (2019)
2. D. Wen, J.J. Cadusch, J. Meng, K.B. Crozier, Light field on a chip: metasurface-based multicolor holograms. Adv. Photonics **3**, 024001 (2021)
3. L. Huang, S. Zhang, T. Zentgraf, Metasurface holography: from fundamentals to applications. Nanophotonics **7**, 1169–1190 (2018)
4. W. Wan, J. Gao, X. Yang, Metasurface holograms for holographic imaging. Adv. Opt. Mater. **5**, 1700541 (2017)
5. W. Song, X. Liang, S. Li, D. Li, R. Paniagua-Domínguez, K.H. Lai, Q. Lin, Y. Zheng, A.I. Kuznetsov, Large-scale Huygens' metasurfaces for holographic 3D near-eye displays. Laser Photonics Rev. **15**, 2000538 (2021)
6. Y. Shi, C. Wan, C. Dai, Z. Wang, S. Wan, G. Zheng, S. Zhang, Z. Li, Augmented reality enabled by on-chip meta-holography multiplexing. Laser Photonics Rev. **16**, 2100638 (2022)
7. J.H. Park, B. Lee, Holographic techniques for augmented reality and virtual reality near-eye displays. Light Adv. Manuf. **3**, 137–150 (2022)
8. Z. Liu, D. Wang, H. Gao, M. Li, H. Zhou, C. Zhang, Metasurface-enabled augmented reality display: a review. Adv. Photonics **5**, 034001 (2023)
9. B.C. Kress, M. Pace, Holographic optics in planar optical systems for next generation small form factor mixed reality headsets. Light Adv. Manuf. **3**, 771–801 (2022)
10. D. Cheng, Q. Wang, Y. Liu, H. Chen, D. Ni, X. Wang, C. Yao, Q. Hou, W. Hou, G. Luo, Y. Wang, Design and manufacture AR head-mounted displays: a review and outlook. Light Adv. Manuf. **2**, 350–369 (2021)
11. Y. Yang, J. Seong, M. Choi, J. Park, G. Kim, H. Kim, J. Jeong, C. Jung, J. Kim, G. Jeon, K.I. Lee, D.H. Yoon, J. Rho, Integrated metasurfaces for re-envisioning a near-future disruptive optical platform. Light Sci. Appl. **12**, 152 (2023)
12. J. Kim, D. Jeon, J. Seong, T. Badloe, N. Jeon, G. Kim, J. Kim, S. Baek, J.L. Lee, J. Rho, Photonic encryption platform via dual-band vectorial metaholograms in the ultraviolet and visible. ACS Nano **16**, 3546–3553 (2022)

13. I. Kim, J. Jang, G. Kim, J. Lee, T. Badloe, J. Mun, J. Rho, Pixelated bifunctional metasurface-driven dynamic vectorial holographic color prints for photonic security platform. Nat. Commun. **12**, 3614 (2021)

14. M.Q. Mehmood, J. Seong, M.A. Naveed, J. Kim, M. Zubair, K. Riaz, Y. Massoud, J. Rho, Single-cell-driven tri-channel encryption meta-displays. Adv. Sci. **9**, 2203962 (2022)

15. T. Naeem, J. Kim, H.S. Khaliq, J. Seong, M.T.S. Chani, T. Tauqeer, M.Q. Mehmood, Y. Massoud, J. Rho, Dynamic chiral metasurfaces for broadband phase-gradient holographic displays. Adv. Opt. Mater. **11**, 2202278 (2023)

16. F. Yue, C. Zhang, X.F. Zang, D. Wen, B.D. Gerardot, S. Zhang, X. Chen, High-resolution grayscale image hidden in a laser beam. Light Sci. Appl. **7**, 17129 (2018)

17. K. Huang, J. Deng, H.S. Leong, S.L.K. Yap, R.B. Yang, J. Teng, H. Liu, Ultraviolet metasurfaces of ≈80% efficiency with antiferromagnetic resonances for optical vectorial anti-counterfeiting. Laser Photonics Rev. **13**, 1800289 (2019)

18. G. Ruffato, R. Rossi, M. Massari, E. Mafakheri, P. Capaldo, F. Romanato, Design, fabrication and characterization of computer generated holograms for anti-counterfeiting applications using OAM beams as light decoders. Sci. Rep. **7**, 18011 (2017)

19. L. Deng, J. Deng, Z. Guan, J. Tao, Y. Chen, Y. Yang, D. Zhang, J. Tang, Z. Li, Z. Li, Malus-metasurface-assisted polarization multiplexing. Light Sci. Appl. **9**, 101 (2020)

20. R. Zhao, L. Huang, Y. Wang, Recent advances in multi-dimensional metasurfaces holographic technologies. PhotoniX **1**, 1–24 (2020)

21. S. Chen, Z. Li, W. Liu, H. Cheng, J. Tian, From single-dimensional to multidimensional manipulation of optical waves with metasurfaces. Adv. Mater. **31**, 1802458 (2019)

22. J. Kim, J. Seong, Y. Yang, S. Moon, T. Badloe, J. Rho, Tunable metasurfaces towards versatile metalenses and metaholograms: a review. Adv. Photonics **4**, 024001 (2022)

23. K. Du, H. Barkaoui, X. Zhang, L. Jin, Q. Song, S. Xiao, Optical metasurfaces towards multifunctionality and tunability. Nanophotonics **11**, 1761–1781 (2022)

24. J.P. Balthasar Mueller, N.A. Rubin, R.C. Devlin, B. Groever, F. Capasso, Metasurface polarization optics: independent phase control of arbitrary orthogonal states of polarization. Phys. Rev. Lett. **118**, 113901 (2017)

25. C. Zhang, S. Divitt, Q. Fan, W. Zhu, A. Agrawal, Y. Lu, T. Xu, H.J. Lezec, Low-loss metasurface optics down to the deep ultraviolet region. Light Sci. Appl. **9**, 55 (2020)

26. A. Arbabi, Y. Horie, M. Bagheri, A. Faraon, Dielectric metasurfaces for complete control of phase and polarization with subwavelength spatial resolution and high transmission. Nat. Nanotechnol. **10**, 937–943 (2015)

27. Q. Song, M. Odeh, J. Zuniga-Perez, B. Kante, P. Genevet, Plasmonic topological metasurface by encircling an exceptional point. Science **373**, 1133–1137 (2021)

28. B. Xiong, Y. Liu, Y. Xu, L. Deng, C.W. Chen, J.N. Wang, R. Peng, Y. Lai, Y. Liu, M. Wang, Breaking the limitation of polarization multiplexing in optical metasurfaces with engineered noise. Science **379**, 294–299 (2023)

29. S.M. Kamali, E. Arbabi, A. Arbabi, Y. Horie, M. Faraji-Dana, A. Faraon, Angle-multiplexed metasurfaces: encoding independent wavefronts in a single metasurface under different illumination angles. Phys. Rev. X **7**, 041056 (2017)

30. S. Latif, J. Kim, H.S. Khaliq, N. Mahmood, M.A. Ansari, X. Chen, J. Akbar, T. Badloe, M. Zubair, Y. Massoud, M.Q. Mehmood, J. Rho, Spin-selective angular dispersion control in dielectric metasurfaces for multichannel meta-holographic displays. Nano Lett. **24**, 708–714 (2024)

31. J. Jang, G.Y. Lee, J. Sung, B. Lee, Independent multichannel wavefront modulation for angle multiplexed meta-holograms. Adv. Opt. Mater. **9**, 2100678 (2021)

32. Z. Shi, M. Khorasaninejad, Y.W. Huang, C. Roques-Carmes, A.Y. Zhu, W.T. Chen, V. Sanjeev, Z.W. Ding, M. Tamagnone, K. Chaudhary, R.C. Devlin, C.W. Qiu, F. Capasso, Single-layer metasurface with controllable multiwavelength functions. Nano Lett. **18**, 2420–2427 (2018)

33. H. Li, X. Xiao, B. Fang, S. Gao, Z. Wang, C. Chen, Y. Zhao, S. Zhu, T. Li, Band-pass-filter-integrated multiwavelength achromatic metalens. Photonics Res. **9**, 1384–1390 (2021)

34. Z. Li, P. Lin, Y.W. Huang, J.S. Park, W.T. Chen, Z. Shi, C.W. Qiu, J.X. Cheng, F. Capasso, Meta-optics achieves RGB-achromatic focusing for virtual reality. Sci. Adv. **7**, 4458 (2021)

35. Z. Li, R. Pestourie, J.S. Park, Y.W. Huang, S.G. Johnson, F. Capasso, Inverse design enables large-scale high-performance meta-optics reshaping virtual reality. Nat. Commun. **13**, 2409 (2022)

36. H. Ren, X. Fang, J. Jang, J. Burger, J. Rho, S.A. Maier, Complex-amplitude metasurface-based orbital angular momentum holography in momentum space. Nat. Nanotechnol. **15**, 948–955 (2020)

37. H. Ren, G. Briere, X. Fang, P. Ni, R. Sawant, S. Heron, S. Chenot, S. Vezian, B. Damilano, V. Brandli, S.A. Maier, P. Genevet, Metasurface orbital angular momentum holography. Nat. Commun. **10**, 2986 (2019)

38. X. Fang, H. Ren, M. Gu, Orbital angular momentum holography for high-security encryption. Nat. Photonics **14**, 102–108 (2019)

39. X. Zhang, M. Pu, Y. Guo, J. Jin, X. Li, X. Ma, J. Luo, C. Wang, X. Luo, Colorful metahologram with independently controlled images in transmission and reflection spaces. Adv. Funct. Mater. **29**, 1809145 (2019)

40. X. Zhang, J. Jin, M. Pu, X. Li, X. Ma, P. Gao, Z. Zhao, Y. Wang, C. Wang, X. Luo, Ultrahigh-capacity dynamic holographic displays via anisotropic nanoholes. Nanoscale **9**, 1409–1415 (2017)

41. D. Wen, F. Yue, G. Li, G. Zheng, K. Chan, S. Chen, M. Chen, K.F. Li, P.W.H. Wong, K.W. Cheah, E. Yue Bun Pun, S. Zhang, X. Chen, Helicity multiplexed broadband metasurface holograms. Nat. Commun. **6**, 8241 (2015)

42. C. Zhang, L. Chen, Z. Lin, J. Song, D. Wang, M. Li, O. Koksal, Z. Wang, G. Spektor, D. Carlson, H.J. Lezec, W. Zhu, S. Papp, A. Agrawal, Tantalum pentoxide: a new material platform for high-performance dielectric metasurface optics in the ultraviolet and visible region. Light Sci. Appl. **13**, 23 (2024)

43. A. Asad, J. Kim, H.S. Khaliq, N. Mahmood, J. Akbar, M.T.S. Chani, Y. Kim, D. Jeon, M. Zubair, M.Q. Mehmood, Y. Massoud, J. Rho, Spin-isolated ultraviolet-visible dynamic meta-holographic displays with liquid crystal modulators. Nanoscale Horiz. **8**, 759–766 (2023)

44. S. So, J. Mun, J. Park, J. Rho, Revisiting the design strategies for metasurfaces: fundamental physics, optimization, and beyond. Adv. Mater. **35**, 2206399 (2023)

45. R. Azzam, Phase shifts that accompany total internal reflection at a dielectric-dielectric interface. J. Opt. Soc. Am. A **21**, 1559–1563 (2004)

46. J. Shi, W. Qiao, J. Hua, R. Li, L. Chen, Spatial multiplexing holographic combiner for glasses-free augmented reality. Nanophotonics **9**, 3003–3010 (2020)

47. J. Hua, W. Qiao, L. Chen, Recent advances in planar optics-based glasses-free 3D displays. Front. Nanotechnol. **4**, 829011 (2022)

48. M. Ozaki, J. Kato, S. Kawata, Surface-plasmon holography with white-light illumination. Science **332**, 218–220 (2011)

49. R. Sprengard, High-index glass wafers open a path to mass-marketing AR glasses. Inf. Disp. **36**, 30–33 (2020)

50. U. Fotheringham, U. Petzold, S. Ritter, W. James, Optical glass and optical design: Otto Schott´s role in the entangled development. Opt. Mater. Express **12**, 3171–3186 (2022)

51. M.S. Soskin, V.N. Gorshkov, M.V. Vasnetsov, J.T. Malos, N.R. Heckenberg, Topological charge and angular momentum of light beams carrying optical vortices. Phys. Rev. A **56**, 4064–4075 (1997)